Wideband Pixel-Based Fluid Antenna System: An Antenna Design for Smart City

Baiyang Liu, Tuo Wu, Kai-Kit Wong, *Fellow, IEEE*, Hang Wong, *Fellow, IEEE*, Kin-Fai Tong, *Fellow, IEEE*

***Abstract*—Smart cities demand versatile antenna systems supporting heterogeneous wireless applications across diverse propagation environments. This paper presents a wideband pixel-based fluid antenna system (PB-FAS) designed as a general-purpose antenna solution for smart city infrastructures, addressing fundamental challenges in wideband operation, spatial adaptability, interference mitigation, and scalable deployment. The proposed PB-FAS integrates parasitic elements for enhanced bandwidth (6.0-7.0 GHz) and a compact 6-PIN-diode pixel surface enabling 64 distinct fluid states, achieving optimal cost-performance balance. An integrated FPGA-based control system provides microsecond-level reconfiguration for real-time channel adaptation. We establish a rigorous exact spatial geometry (ESG) channel model capturing state-dependent antenna responses across near-field and far-field regions, providing a unified theoretical foundation for interference mitigation analysis. Comprehensive validation through full-wave electromagnetic simulations, anechoic chamber measurements, and experimental two-source 16-QAM communication tests demonstrates up to 11 dB SINR improvement and 13.2% EVM reduction through hardware-level spatial diversity, confirming the system's effectiveness as a scalable, cost-effective solution for next-generation smart city wireless infrastructures ranging from IoT sensor networks to high-capacity backhaul links.**

***Index Terms*—Smart city, fluid antenna system (FAS), pixel-based fluid antenna, wideband antenna, interference mitigation, spatial diversity, IoT communication.**

I. Introduction

THE sixth-generation (6G) wireless communication systems are anticipated to meet unprecedented requirements for high data rates, ultra-low latency, and spectral efficiency exceeding 1000 bits per second per Hertz (bps/Hz) to support emerging applications such as immersive extended reality, holographic communications, and autonomous systems [1]–[4]. The rapid evolution of smart cities further demands versatile wireless communication infrastructures capable of supporting diverse applications ranging from autonomous vehicles and IoT sensor networks to augmented reality and industrial automation [5]–[7]. These heterogeneous systems operate across various frequency bands, power levels, and mobility patterns, creating complex electromagnetic environments with dynamic interference patterns and varying channel conditions [8]–[10]. Conventional multiple-input multiple-output (MIMO) architectures, despite their proven effectiveness in current networks, exhibit inherent limitations in scalability and adaptability for 6G and smart city scenarios due to their reliance on fixed physical structures with limited reconfiguration capabilities [11]–[13]. Traditional fixed-pattern antennas, while reliable, lack the adaptability required to optimize performance across such diverse deployment scenarios [7], [14].

Fluid antenna systems (FAS), also known as movable antenna systems, have recently emerged as a paradigm-shifting technology that addresses these fundamental limitations through physically fluid antenna structures [15], [16]. By enabling dynamic port selection and position optimization within a constrained physical space, FAS fundamentally decouples the radiation characteristics from fixed hardware constraints, thereby facilitating adaptive spatial multiplexing and diversity exploitation. FAS represent a paradigm shift from conventional multi-antenna approaches by offering spatial adaptability through dynamic repositioning—either physical or virtual—within a predefined region. In an FAS, the position of the radiating element can be dynamically reconfigured across a spatial aperture, enabling flexible and adaptive control over the antenna's spatial behavior. This reconfigurability can be achieved through various means—such as electronically switchable pixel arrays [17]–[20], liquid metal [16], [21], mechanical actuators [22], or advanced metasurfaces [23]—without necessarily requiring any physical displacement or fluidic materials. By allowing the effective radiation point to change in response to the environment or communication needs, FAS unlock additional spatial degrees of freedom, offering new opportunities for enhancing performance in next-generation wireless systems. This capability enables real-time optimization of radiation patterns based on instantaneous channel conditions, providing interference mitigation, multi-user discrimination, and enhanced spatial diversity using only a single RF chain. Recent investigations have demonstrated FAS's potential advantages in various aspects of wireless communications, including capacity enhancement, reliability improvement, and resource utilization optimization [24]–[31].

Unlike traditional MIMO systems, FAS achieves diversity gains purely at the hardware level, offering significant cost and complexity reductions essential for large-scale smart city deployments. Among the various FAS implementation approaches, electronically switchable pixel-based systems [15], [32]–[37] stand out for their fast switching speeds, compact form factors, and suitability for integration into urban infrastructure, making them particularly attractive for massive connectivity scenarios such as Internet of Things (IoT) [38],

This research work of K. F. Tong was funded by Hong Kong Metropolitan University, Staff Research Startup Fund: FRSF/2024/03. The work of T. Wu, H. Wong was funded by Hong Kong ResearchGrants Council under the Area of Excellence Scheme under Grant AoE/E-101/23-N.

B. Liu is with the School of Science and Technology, Hong Kong Metropolitan University, Hong Kong, China, and also with the School of Artificial Intelligence, Shenzhen Technology University, Shenzhen, China. T. Wu, and H. Wong are with the State Key Laboratory of Terahertz and Millimeter Waves, City University of Hong Kong, Hong Kong, China. K.-K. Wong is with the Department of Electronic and Electrical Engineering, University College London, London, UK. K.-F. Tong is with the School of Science and Technology, Hong Kong Metropolitan University, Hong Kong, China (E-mail: ktong@hkmu.edu.hk).

Baiyang Liu, Tuo Wu contributed equally to this work.

(*Corresponding author: Kin-Fai Tong.*)

[39], where power and computational resources are limited.

However, early FAS implementations face significant challenges in smart city applications. Mechanical repositioning systems suffer from slow switching speeds, limited durability, and integration difficulties in compact urban infrastructure [21]. Meanwhile, existing pixel-based fluid antennas (PRAs), while electronically switchable, are typically constrained to narrow frequency bands (e.g., 2.4-2.6 GHz with $< 3\%$ bandwidth), limited state numbers (≈ 12), and lack integrated control systems [20]. These limitations severely restrict their applicability in smart city environments where wideband operation, numerous reconfigurable states, and autonomous control are essential requirements. Furthermore, meta-fluid antennas [7], [40], which integrate large-scale diode-controlled metasurfaces, offer finer spatial control but require dozens to hundreds of PIN diodes, leading to high cost, high power consumption, and complex biasing circuitry, which are prohibitive for scalable deployment.

Smart city applications demand antenna systems that can seamlessly operate across multiple frequency bands (sub-7 GHz for coverage, higher frequencies for capacity), adapt to diverse propagation environments (urban canyons, open spaces, indoor/outdoor transitions), and support heterogeneous device requirements (low-power IoT sensors, high-data-rate applications, mobile users). Furthermore, the massive scale of smart city deployments necessitates cost-effective, energy-efficient solutions that can be easily integrated into existing infrastructure while providing reliable performance across varying environmental conditions.

Achieving such a comprehensive antenna solution presents significant technical challenges. The fundamental difficulty lies in simultaneously satisfying multiple conflicting design objectives: wideband impedance matching inherently conflicts with compact form factor requirements, as traditional bandwidth enhancement techniques (e.g., stacked patches, thick substrates) increase antenna volume. Rich state diversity typically demands numerous switching elements, escalating hardware complexity, power consumption, and manufacturing costs. Real-time reconfiguration requires not only fast switching hardware but also integrated control systems with minimal latency, which are challenging to integrate within space-constrained antenna structures. Moreover, achieving spatial diversity across varied propagation environments necessitates generating truly distinct radiation patterns rather than merely perturbing existing ones—a requirement that conventional reconfigurable designs struggle to meet while maintaining consistent impedance matching across all states.

To address these multifaceted challenges, this paper presents a comprehensive wideband pixel-based fluid antenna system (PB-FAS) design and validation framework that systematically tackles the theoretical, hardware, and experimental complexities associated with smart city antenna deployment. We develop a novel antenna architecture integrating parasitic elements for wideband operation (6.0-7.0 GHz) and a compact 6-PIN-diode pixel surface enabling 64 distinct fluid states with optimal cost-performance trade-off. We establish a rigorous exact spatial geometry (ESG) channel model that accurately captures state-dependent electromagnetic responses across near-field and far-field regions, providing a unified theoretical foundation for FAS-based interference mitigation analysis. We implement an integrated FPGA-based control system achieving microsecond-level reconfiguration with 20 MHz system clock for real-time channel adaptation. We validate our framework through comprehensive full-wave electromagnetic simulations, anechoic chamber measurements, and experimental demonstrations in realistic two-source interference scenarios at 6.8 GHz, achieving up to 11 dB SINR improvement and 13.2% EVM reduction. The conceptual illustration of this system is presented in Fig. 1, where both transmitters and the receiver are equipped with the PB-FAS, transmitting different signals over a rich scattering environment with dynamically fluid antenna states at both ends for effective interference mitigation. This work's primary contributions are summarized as follows:

- ***Wideband Pixel-Based Fluid Antenna System***—We introduce a novel PB-FAS design that achieves wideband operation (6.0-7.0 GHz) through strategic integration of parasitic elements while maintaining compact form factor. Unlike conventional narrow-band fluid antennas ($<$ 3% bandwidth) or complex meta-fluid systems requiring hundreds of PIN diodes, our architecture employs only 6 PIN diodes controlling 36 pixel patches to create 64 distinct fluid states. We specifically develop a parasitic-enhanced impedance matching technique that ensures reliable matching across all reconfigurable states, addressing the fundamental conflict between bandwidth enhancement and state diversity.
- ***Unified Exact Spatial Geometry Channel Model***—We establish a rigorous ESG theoretical framework that accurately models state-dependent antenna responses across both near-field and far-field regions. Our model captures the fundamental physics of pixel-based reconfiguration, where PIN diode switching redistributes surface currents and modulates the effective radiating aperture.
- ***Hardware-Level Spatial Diversity and Interference Mitigation***—We demonstrate that substantial interference suppression and spatial diversity gains can be achieved purely through antenna-level reconfiguration without requiring multiple RF chains or complex baseband signal processing. Our approach fundamentally differs from traditional MIMO systems by exploiting electromagnetic reconfigurability at the hardware level, dramatically reducing system complexity while eliminating the need for computationally intensive precoding, equalization, or channel estimation algorithms—particularly advantageous for resource-constrained IoT devices in smart city deployments.
- ***Comprehensive Multi-Domain Validation***—We present thorough validation spanning electromagnetic characterization, communication performance evaluation, and practical implementation feasibility. Our validation includes full-wave simulations of all 64 fluid states, anechoic chamber measurements of reflection coefficients and radiation patterns, near-field distribution analysis revealing spatial diversity mechanisms, and experimental two-

source 16-QAM communication tests demonstrating 11 dB SINR improvement and 13.2% EVM reduction. This multi-faceted validation confirms both the electromagnetic integrity and communication-level effectiveness of the proposed system.

- ***General-Purpose Smart City Antenna Solution***—Our analysis and experimental results reveal that PB-FAS offers a scalable, cost-effective solution addressing the diverse and demanding requirements of smart city wireless infrastructures. We provide practical design guidelines for achieving simultaneous wideband operation, rich state diversity, fast reconfiguration, and compact integration—enabling a single antenna platform to serve heterogeneous applications ranging from low-power IoT sensor networks requiring interference resilience to high-capacity backhaul links demanding spatial selectivity, thereby reducing deployment complexity and lifecycle costs in large-scale smart city infrastructures.

The proposed PB-FAS achieves wideband operation (6.0–7.0 GHz) through parasitic-enhanced matching, while the earlier PRA [20] remained narrow-band ($<3\%$) and only 12 available states. The design significantly reduces component complexity by employing only 6 PIN diodes to control 36 pixel patches, resulting in 64 distinct reconfigurable states with low cost and high reliability. Moreover, an integrated FPGA controller enables microsecond-level real-time switching for adaptive interference mitigation, achieving up to 11 dB SINR improvement and 13.2% EVM reduction—capabilities not demonstrated in the previous PRA. The compact, low-power PB-FAS design is also highly scalable for dense IoT deployments in smart-city environments. Its current limitations include a smaller number of reconfigurable states compared with metasurface arrays and minor switching losses from PIN-diode parasitics, which may slightly affect radiation efficiency. The comparison between our work and other FAS related studies with experimental results is presented in Table I.

In smart city networks, the IoT plays a central role by interconnecting vast numbers of devices supporting applications such as intelligent transportation, environmental monitoring, energy management, healthcare, and public safety. These IoT nodes often operate in dense environments where multiple wireless systems share overlapping frequency bands, leading to severe co-channel interference and degraded link reliability. Achieving robust and efficient multiplexing among such heterogeneous devices is therefore a fundamental challenge. The proposed PB-FAS provides a hardware-level solution to these issues by dynamically reconfiguring its radiation state to adapt to interference conditions in real time. Through spatial pattern diversity and reconfigurable beam control, PB-FAS can selectively enhance desired links while suppressing unwanted interference, enabling spectrum-efficient and interference-resilient communication for large-scale IoT deployments across smart city infrastructures.

II. System Model

This section presents the system architecture and establishes a rigorous theoretical foundation for wireless systems employing the proposed PB-FAS.

A. System Architecture Overview

The proposed PB-FAS communication system enables interference mitigation through coordinated fluid antenna states at both transmitter and receiver ends. As illustrated in Fig. 1, the system consists of multiple transceivers operating in a rich scattering environment, where each terminal is equipped with a wideband pixel-based antenna capable of 64 distinct fluid states.

The key system components include: (1) **Transmitters (Tx1, Tx2)**: Each equipped with a PB-FAS antenna and FPGA-based control board for real-time state switching at 20 MHz speed; (2) **Receiver (Rx)**: Similarly equipped with PB-FAS for adaptive spatial filtering; (3) **Rich Scattering Environment**: Urban/indoor scenarios with multiple scatterers that create multipath propagation; (4) **Control System**: FPGA-based controllers enable microsecond-level state reconfiguration for dynamic interference nulling.

The system operates by dynamically selecting optimal antenna states to maximize the desired signal strength while spatially suppressing interference. Unlike traditional MIMO systems that require multiple RF chains and complex signal processing, this approach achieves spatial diversity purely through hardware-level antenna reconfiguration, making it particularly suitable for resource-constrained IoT applications.

Remark 1: Accurately modeling the communication channel is paramount, especially for a fluid antenna whose properties change dynamically. The uniqueness of the PB-FAS lies in its ability to rapidly alter its fundamental electromagnetic characteristics by reconfiguring the PIN diode connections on the pixel surface. This electronic switching fundamentally changes the distribution paths of currents on the antenna surface, which in turn reshapes the phase and amplitude distribution of the radiated electromagnetic field and, consequently, the effective radiation direction and beam shape. This rapid reconfiguration of the antenna's physical current paths means its *effective radiating aperture* is state-dependent.

To accurately model the PB-FAS system described above, we must first understand how the state-dependent nature of the antenna affects the fundamental electromagnetic field regions. The dynamic reconfiguration capability highlighted in the system architecture directly impacts the spatial characteristics of the radiated field, necessitating a rigorous analysis of how different pixel states influence the near-field and far-field boundaries.

B. Field Regions and State-Dependent Wavefronts

The interaction between an antenna and a source is governed by the distance r relative to the antenna's effective aperture, D. For the PB-FAS, the effective aperture can be considered state-dependent, denoted as $D(s)$, as different pixel configurations alter the radiating current distribution. This defines state-dependent field regions:

- **Far-Field (Fraunhofer) Region:** For distances $r > R_F(s)$, where $R_F(s) = \dfrac{2D(s)^2}{\lambda}$ is the state-dependent Rayleigh distance. In this region, the electromagnetic wave can be approximated as a planar wavefront.

TABLE I
COMPARISON BETWEEN THE PROPOSED PB-FAS AND RECENT FLUID ANTENNA DESIGNS

Work	Freq. (GHz)	No. of States	BW (%)	Switching	Key Features / Limitations
Suzuki *et al.* 2022 [41]	60 GHz	Theoretically continuous, but limited by the width of the clothespin	1.76 over 60 GHz band, 2.93%	Very slow. Manually clip to shift radiating points	Enables dynamic position reconfiguration for better signal diversity, but limited by mechanical delay, maintenance, and hardware durability issues.
Dong *et al.* 2024 [42]	3.5 GHz and 27.5 GHz depending of the antenna element used	Continuous	400MHz, about 11% and 1.45%	Mechanical movement using electric motors	Converts dielectric waveguide into leaky antenna for localized links; limited by primitive setup, imprecise control, unclear activation, and no multi-user validation.
Shen *et al.* 2024 [21]	24–30	Continuous	∼8	Mechanical / slow	Surface-wave fluid antenna; first mmWave demonstration of Fluid Antenna Multiple Access (FAMA); high gain (≈11 dBi) but limited reconfiguration speed due to liquid motion.
Zhang *et al.* 2024 [20]	2.5	12 (6 PIN)	∼3	μs (RF switch)	Pixel-based reconfigurable antenna applied in fluid antenna systems; compact $0.67\lambda \times 0.67\lambda$ aperture; fast electronic switching; narrowband response and limited spatial diversity.
Liu *et al.* 2025 [7]	26.5	2^{120} (480 PIN)	n.a.	μs (FPGA)	Programmable meta-fluid antenna using metasurface coding; demonstrated spatial multiplexing and interference exploitation; complex fabrication and high design cost.
This Work (PB-FAS)	**6.0–7.0**	**64 (6 PIN)**	**∼15**	**20 MHz (FPGA)**	**Both Ends pixel–fluid architecture; wideband parasitic-enhanced impedance matching; 11 dB SINR & 13.2% EVM improvement; compact, low-cost, IoT-oriented interference-mitigation design.**

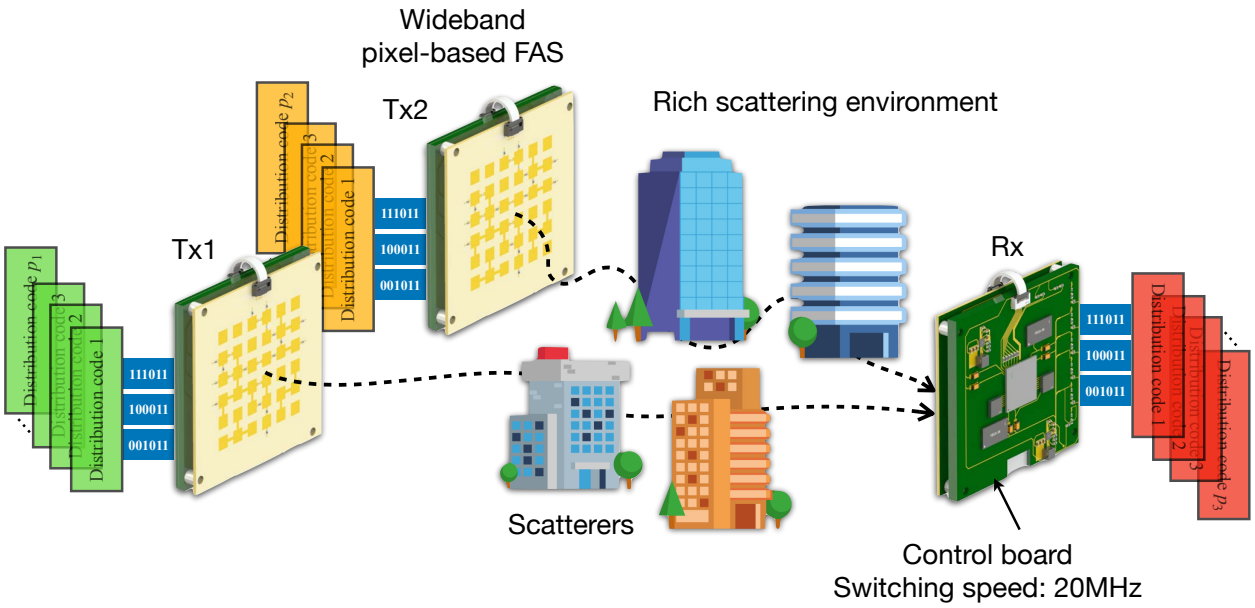

Fig. 1. Conceptual illustration of the proposed PB-FAS for interference mitigation. Two transmitters equipped with wideband PB-FAS antennas transmit distinct signals through a rich scattering environment. The receiver, also equipped with a PB-FAS, dynamically reconfigures its radiation state in coordination with the transmitters to suppress interference and enhance signal quality. The system supports real-time adaptation at both ends through hardware-level pixel-state control.

- **Near-Field (Fresnel) Region:** For distances within the Rayleigh distance, the spherical nature of the wavefront must be considered, as the planar approximation becomes inaccurate.

The experiments in this work are conducted in an indoor environment where the transmitter-receiver distance is several meters. Given the antenna's compact size ($D \approx 7\,\text{cm}$) and the operating frequency of 6.8 GHz ($\lambda \approx 4.4\,\text{cm}$), the Rayleigh distance is approximately 0.22 m. Therefore, our experimental validation operates within the far-field region. However, a general model should encompass all scenarios.

Having established the state-dependent field regions, we now develop a mathematical framework that can accurately represent the antenna's response across all these regions. The following unified model captures the complex electromagnetic

behavior of the PB-FAS system and serves as the basis for the interference mitigation algorithms described in the system architecture.

C. A Unified Steering Vector Model for PB-FAS

To provide a comprehensive framework, we introduce an exact spatial geometry (ESG) model that is valid across all field regions. The ESG steering vector, $\mathbf{a}^{\text{ESG}}(\theta, r, s)$, represents the true, complex response of the antenna in state s to a source at angle θ and distance r. This vector can be obtained through full-wave electromagnetic simulations (as seen in the near-field analysis in Fig. 5) or calibrated measurements. The ESG model can be conceptually understood as follows, though its exact form for a pixel antenna is complex:

$$\mathbf{a}^{\text{ESG}}(\theta, r, s) \propto \left[\frac{r}{r_1(s)} e^{j\frac{2\pi}{\lambda}(r_1(s)-r)}, \ldots, \frac{r}{r_N(s)} e^{j\frac{2\pi}{\lambda}(r_N(s)-r)} \right]^T \quad (1)$$

where $r_m(s)$ represents the distance from the source to the m-th effective radiating point of the pixel surface in state s. This unified model degenerates to simpler forms under certain approximations.

1) Far-Field Approximation: In the far-field ($r \gg R_F(s)$), the wavefront is planar, and the distance from the source to an effective radiating point $p_m(s)$ can be approximated using the first-order Taylor expansion, which is given by

$$r_m(s) \approx r - p_m(s) \sin\theta. \quad (2)$$

Under this approximation, the amplitude term $\frac{r}{r_m(s)} \to 1$, and the phase term in the ESG model simplifies. The steering vector becomes $\mathbf{a}^{\text{FF}}(\theta, s)$, which primarily depends on the angle of arrival θ and the state s, representing the antenna's far-field radiation pattern for that state.

2) Near-Field Approximation: In the near-field, the planar wavefront assumption is invalid. A more accurate approximation can be obtained by using a second-order Taylor expansion for the distance, which is formulated as

$$r_m(s) \approx r - p_m(s) \sin\theta + \frac{p_m(s)^2 \cos^2\theta}{2r}. \quad (3)$$

This leads to a near-field steering vector, $\mathbf{a}^{\text{NF}}(\theta, r, s)$, which includes a quadratic phase term that depends on both angle and range. While more accurate than the far-field model, such approximations can still introduce errors, especially near the field boundaries. Our analysis therefore relies on the full ESG model or its valid far-field representation for the experimental scenario.

With the unified steering vector model established, we can now formulate the complete channel model for the PB-FAS communication system. This model incorporates the state-dependent antenna responses into the multipath channel representation, enabling accurate prediction of system performance under various interference scenarios.

D. Channel Model with PB-FAS

Let the transmitter and receiver PB-FAS support S_{TX} and S_{RX} unique fluid states, respectively. For any selected state pair $(s_{\text{TX}}, s_{\text{RX}})$, the baseband equivalent channel is expressed as:

$$y = h_{s_{\text{TX}}, s_{\text{RX}}} \cdot x + n \quad (4)$$

where x is the transmitted symbol, y is the received symbol, and $n \sim \mathcal{CN}(0, \sigma^2)$ is additive white Gaussian noise. Assuming a geometric multipath channel with L resolvable components, the effective channel gain $h_{s_{\text{TX}}, s_{\text{RX}}}$ is represented using the ESG model:

$$h_{s_{\text{TX}}, s_{\text{RX}}} = \sum_{l=1}^{L} \gamma_l \cdot (\mathbf{a}_{\text{TX}}^{\text{ESG}}(\theta_l, r_l, s_{\text{TX}}))^H \cdot \mathbf{a}_{\text{RX}}^{\text{ESG}}(\theta_l, r_l, s_{\text{RX}}) \quad (5)$$

where γ_l is the complex gain of the l-th path, and $\mathbf{a}^{\text{ESG}}(\cdot)$ is the state-dependent ESG response vector of the transmitter or receiver antenna for that path.

To demonstrate the practical application of the developed channel model, we now consider a specific interference scenario that directly relates to the system architecture presented earlier. This two-source downlink scenario represents a common deployment case where the PB-FAS system's interference mitigation capabilities can be effectively utilized.

E. Two-Source Downlink Scenario with Interference

To explore the interference mitigation potential of PB-FAS, consider a downlink system with two transmitters and one receiver, each equipped with a PB-FAS. Transmitter 1 (Tx1) transmits a desired signal x_1, while Transmitter 2 (Tx2) generates an interfering signal x_2. Let $s_{\text{TX},1}, s_{\text{TX},2} \in \{1, \ldots, 64\}$ and $s_{\text{RX}} \in \{1, \ldots, 64\}$ be the selected fluid states. The received signal can be modeled as:

$$y = h_1(s_{\text{TX},1}, s_{\text{RX}}) \cdot x_1 + h_2(s_{\text{TX},2}, s_{\text{RX}}) \cdot x_2 + n \quad (6)$$

where h_1 and h_2 are the effective channels from Tx1 and Tx2 to the receiver, respectively, as defined in the previous subsection. The signal-to-interference-plus-noise ratio (SINR) at the receiver is given by:

$$\text{SINR}(s_{\text{TX},1}, s_{\text{TX},2}, s_{\text{RX}}) = \frac{|h_1(s_{\text{TX},1}, s_{\text{RX}})|^2}{|h_2(s_{\text{TX},2}, s_{\text{RX}})|^2 + \sigma^2} \quad (7)$$

By dynamically selecting the receiver state s_{RX}, the system can search for a configuration that maximizes this SINR, effectively enhancing the desired signal while spatially nulling the interference.

To quantify the reliability of the interference mitigation system described above, we define performance metrics that capture the probability of successful communication under varying channel conditions. These metrics provide a comprehensive assessment of the system's robustness in practical deployment scenarios.

F. Outage Probability

To evaluate communication reliability, define a SINR threshold γ_{th} below which decoding is considered unreliable. The outage probability is defined as:

$$P_{\text{out}} = \Pr\left\{\text{SINR}(s_{\text{TX},1}, s_{\text{TX},2}, s_{\text{RX}}) < \gamma_{\text{th}}\right\} \tag{8}$$

For a discrete set of N_{config} tested state combinations, this probability can be estimated empirically as:

$$\hat{P}_{\text{out}} = \frac{1}{N_{\text{config}}} \sum_{i=1}^{N_{\text{config}}} \mathbb{I}\left\{\text{SINR}_i < \gamma_{\text{th}}\right\} \tag{9}$$

where $\mathbb{I}\{\cdot\}$ is the indicator function. The SINR threshold of $5\,\text{dB}$ is selected based on typical demodulation requirements for moderate-order modulation schemes such as 16-QAM. In practical systems, an SINR above $5\,\text{dB}$ generally ensures a sufficiently low bit error rate (BER) for reliable communication, particularly when combined with forward error correction (FEC). This threshold strikes a balance between being stringent enough to reflect meaningful performance and being practical for interference-limited environments. It also aligns with standard evaluation criteria used in the design and benchmarking of wireless systems operating under fading and spatial interference conditions. The outage probability is then defined as the likelihood that the SINR under a given state configuration falls below this $5\,\text{dB}$ threshold, indicating a failure to maintain reliable communication.

III. Wideband Pixel-Based Fluid Antenna Systems

This section presents the design, fabrication, simulation and measurement data of the proposed wideband PB-FAS, intended for sub-7 GHz applications. The antenna structure combines a driven patch radiator, four parasitic elements and a reconfigurable pixelated surface to achieve both broadband impedance matching and dynamic pattern control.

A. Configuration and Structure

The proposed antenna adopts a stacked configuration, as illustrated in Fig. 2. The middle layer consists of a rectangular microstrip patch radiator fed by a microstrip line. A set of parasitic elements is strategically placed above the main radiator to enhance impedance matching over a wider frequency range. ***Unlike [20], such wideband characteristic is particularly important, as it ensures the acceptable impedance match, i.e., S11 < -10 dB, of the PB-FAS when it switches through the 64 fluid state for the best state.*** The top layer, a reconfigurable pixel surface is implemented, consisting of thirty-six square conductive patches interconnected via six PIN diodes, eleven inductors and three capacitors. The on-off states of PIN diodes are controlled through DC bias lines routed along the antenna's perimeter, enabling 64 distinct fluid states. To ensure rapid state switching, the antenna is integrated with a bias control board based on a low-latency FPGA controller at the bottom layer. This setup allows real-time state reconfiguration, enabling the antenna to dynamically adapt to changing propagation environments. The FPGA supports switching speeds of up to 20 MHz, allowing for fast and frequent updates of the antenna state. This high-speed reconfigurability makes the antenna suitable for adapting to fast-varying wireless channels, such as those encountered in mobile or dense multi-user environments.

B. Fabrication and Prototype

Three prototypes of the proposed PB-FAS were fabricated using standard PCB manufacturing techniques. The top layer contains the pixel elements, PIN diodes, inductors and capacitors, while the middle and bottom layers accommodate the radiator, parasitic elements and ground plane, respectively. One of the assembled prototypes is shown in Fig. 3. The PIN diodes, *MADP-000907-14020P*, used are rated for sub-7 GHz operation and exhibit low insertion loss in the ON state and high isolation in the OFF state. An FPGA-based bias control board is integrated on the backside of the structure, providing high-speed control of the diode switching. The FPGA is powered via a USB cable connected to a power bank.

C. Reflection Coefficient

The reflection coefficient (S_{11}) was measured across all 64 reconfigurable fluid states using a vector network analyzer (VNA). Fig. 4 presents both simulated and measured S_{11} curves for representative states. The comprehensive analysis reveals several key characteristics of the proposed antenna system.

Frequency Tuning Capability: The 64 curves demonstrate distinct resonant frequencies distributed across the 6.0-7.0 GHz range, indicating that different states achieve optimal matching at different frequency points. This frequency diversity enables the system to select the best matching frequency point within the wideband through state switching. Such dynamic frequency selection capability allows the system to choose optimal states based on specific operating frequency requirements, providing enhanced adaptability for wideband applications.

Envelope Boundary Analysis: The orange lines in Fig. 4 represent the upper and lower bounds of S_{11} across all 64 fluid states, serving multiple critical functions. These boundaries define the overall tuning range of the proposed PRA and provide performance guarantees—ensuring that within the 6.0-7.0 GHz range, there is always at least one state that can provide good impedance matching (below -10 dB). This comprehensive coverage demonstrates the robustness of the parasitic-enhanced matching design across the entire operating bandwidth.

Simulation-Measurement Validation: The comparison between Fig. 4(a) and (b) shows excellent overall consistency between simulation and measurement results, validating the reliability of the design methodology. While the measured curves exhibit slightly more variation than simulations—reflecting non-ideal factors in practical manufacturing such as fabrication tolerances and component variations—the fundamental matching characteristics are well preserved. This agreement confirms the effectiveness of the parasitic-enhanced matching design and demonstrates that the theoretical predictions accurately capture the antenna's behavior across all reconfigurable states.

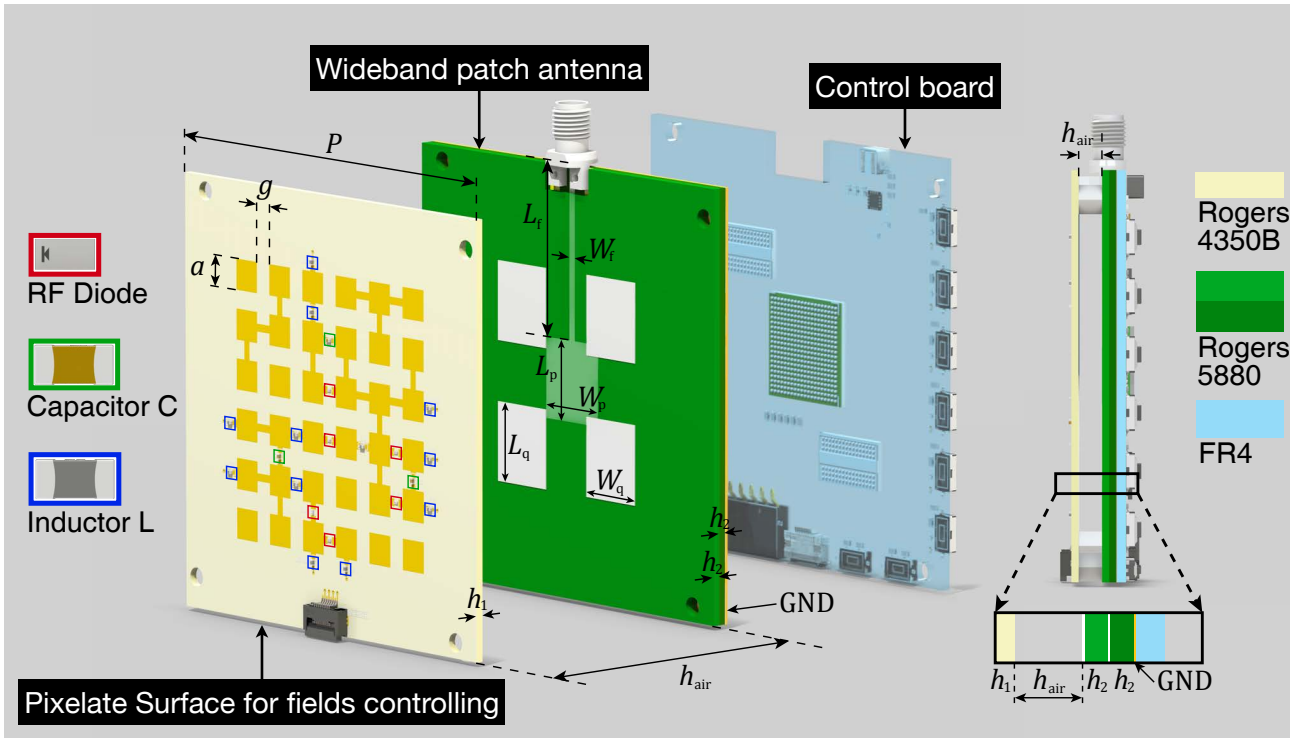

Fig. 2. Configuration of the proposed PB-FAS, showing the driven patch, parasitic elements, and pixel-switching structure. The detailed parameters of the proposed antenna are: $P = 70mm$, $a = 5mm$, $g = 3mm$, $h_1 = 1mm$, $L_f = 28.428mm$, $W_f = 3mm$, $L_p = 13.144mm$, $W_p = 12.309mm$, $L_q = 12.967mm$, $W_q = 11.500mm$, $h_2 = 1.5mm$, $h_{air} = 4mm$.

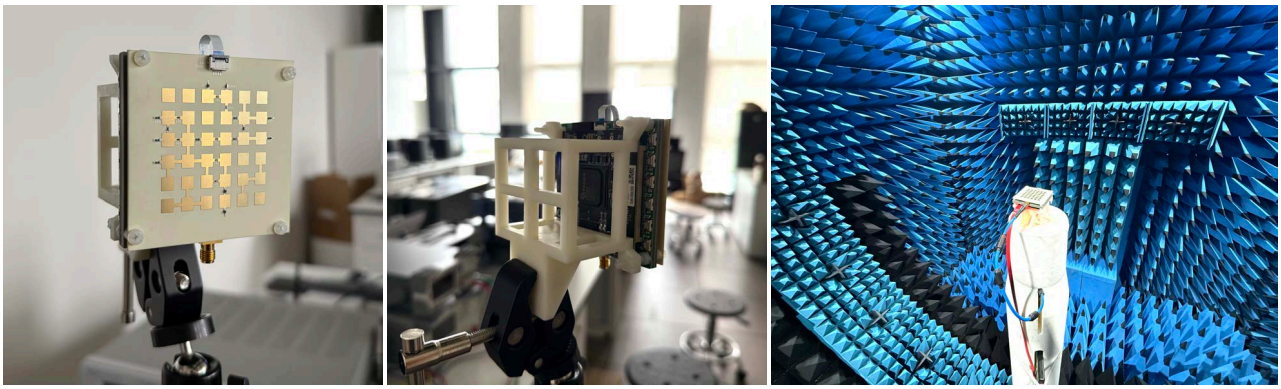

Fig. 3. Photographs of the fabricated PB-FAS prototype and its testing environment. (a) shows the front view of the prototype, highlighting the pixelated antenna surface with integrated PIN diodes and matching components. (b) presents the back view, where a low-latency FPGA controller is integrated for real-time state switching. (c) depicts the prototype under test in an anechoic chamber for radiation patterns measurement.

The minor discrepancies are primarily attributed to the actual impedance variations of PIN diodes in their on-off states and passive component tolerances.

D. Radiation Characteristics

To illustrate the reconfigurable spatial characteristics of the proposed pixel-based antenna, we analyze the near-field distributions generated by all 64 fluid states. Full-wave simulations were performed to extract the amplitude and phase of the electric field at a planar surface located 1λ above the antenna, over a area $3\lambda \times 3\lambda$ centered on the antenna aperture. This analysis provides comprehensive insight into the spatial field diversity enabled by different pixel configurations.

Complete State Space Visualization: Fig. 5 presents all 64 reconfigurable states in an 8×8 grid layout, systematically arranged from binary code 000000 to 111111. Each 6-bit binary code corresponds to the ON/OFF configuration of the six PIN diodes, where '1' indicates forward-biased (ON) and '0' indicates reverse-biased (OFF). This systematic encoding demonstrates the complete utilization of the available switching combinations, with each state producing a distinct electromagnetic signature.

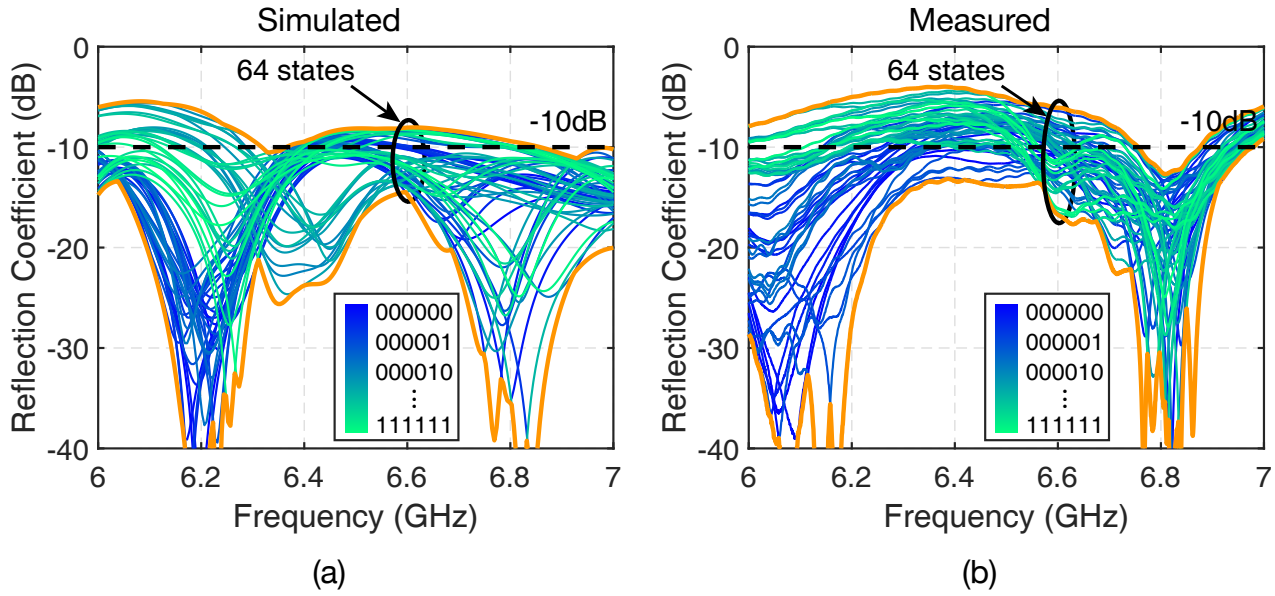

Fig. 4. Simulated and measured S_{11} curves for selected pixel states of the proposed antenna. (a) presents the simulation results obtained using 2024 CST Microwave Studio, and (b) shows the measured results obtained using a vector network analyzer (VNA). The results confirm that the antenna maintains good impedance matching across the sub-7 GHz band for various reconfigurable states.

Near-Field Distribution Diversity: The amplitude distributions in Fig. 5(a) reveal remarkable spatial diversity, with energy concentration patterns varying significantly across states. The color-coded visualization (blue for low amplitude to yellow for high amplitude) shows that different states focus electromagnetic energy in different spatial regions. Similarly, the phase distributions in Fig. 5(b) exhibit diverse wavefront structures, with phase gradients and patterns that are unique to each configuration. This diversity in both amplitude and phase creates a rich spatial basis for interference control and channel adaptation.

PIN Diode Switching Impact: The systematic state progression reveals how individual PIN diode switching affects the overall field distribution. Comparing adjacent states (e.g., 000000 vs 000001) demonstrates the incremental impact of single diode switching, while states with multiple diode differences show cumulative nonlinear effects. This nonlinear response characteristic is crucial for achieving fine-grained spatial control, as small configuration changes can produce significant field redistribution.

Spatial Diversity Foundation: The 64 unique near-field patterns provide the physical foundation for spatial diversity and interference mitigation. No two states exhibit identical field distributions, confirming that each configuration creates a distinct electromagnetic environment. Even visually similar states possess subtle but important differences that translate to significantly different channel responses in rich-scattering environments. This spatial selectivity enables the system to achieve interference nulling and signal enhancement through pure hardware reconfiguration.

Engineering Design Validation: The results validate the effectiveness of the pixel surface design, where 36 conductive patches interconnected via 6 PIN diodes successfully generate diverse radiation modes from a single feed point. The surface current redistribution caused by different switching states effectively modulates the antenna's radiating aperture, confirming the state-dependent aperture concept introduced in the theoretical model. This hardware-level reconfigurability provides a compact alternative to traditional antenna arrays while maintaining rich spatial diversity capabilities.

The radiation pattern measurements were performed in a standard anechoic chamber equipped with a multiple far-field receiving antenna. As shown in Fig. 3 (c), the fabricated PB-FAS was mounted on a platform to capture the E-plane radiation patterns at 6.8 GHz. An external FPGA controller was connected to the antenna to sequentially switch among the 64 pixel states during the measurement procedure.

The radiation patterns of the PB-FAS were simulated and measured in an anechoic chamber. Fig. 6 shows the E-plane patterns at 6.8 GHz. The results demonstrate distinct radiation directions and beam shapes across states, verifying the pixel surface's ability to reconfigure the far-field pattern without changing the feeding structure. The measured patterns closely follow the simulated trends, with minor discrepancies attributed to fabrication tolerance and switch non-idealities.

E. Statement on Similar Radiation Characteristics

Although several fluid states exhibit visually similar characteristics in both the near-field and far-field domains, careful observation reveals subtle differences in their electromagnetic behavior. These slight variations, while not drastically altering beam direction or shape, play a significant role in shaping the wireless channel response—particularly in rich-scattering environments. Such fine-grained diversity among pixel states enables enhanced spatial multiplexing performance beyond what traditional beamforming can achieve. In the following

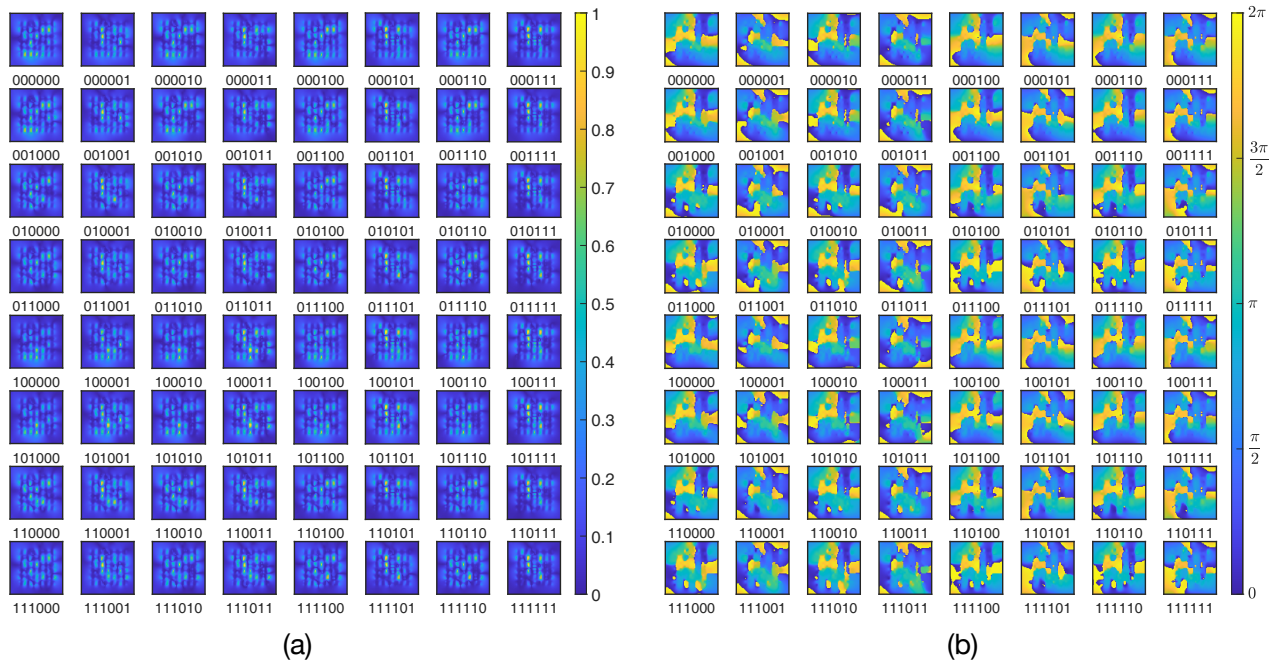

Fig. 5. Simulated near-field distributions at 6.8 GHz for all 64 reconfigurable states. (a) shows the normalized amplitude, and (b) shows the phase distributions. The data is taken at a plane located 1 λ above the antenna aperture, with a sampling area of 3 λ × 3 λ. Each subfigure corresponds to a distinct pixel state, illustrating the spatial field variation and diversity achievable through state reconfiguration. The binary codes represent the configuration states of the 6 PIN diodes, where each bit indicates the ON/OFF status of a diode—1 for forward-biased (ON) and 0 for reverse-biased (OFF).

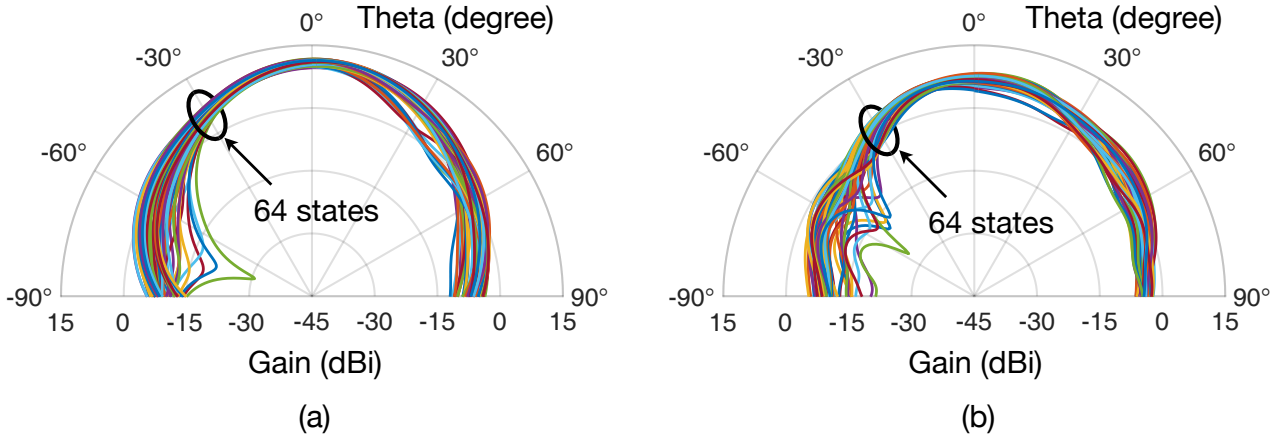

Fig. 6. Simulated and measured E-plane radiation patterns at 6.8 GHz for all 64 pixel states of the proposed antenna. (a) shows the simulated radiation patterns, while (b) presents the measured patterns obtained in an anechoic chamber. The results demonstrate the beam-shaping capability enabled by discrete pixel-state reconfiguration.

Section IV, in Figure 7 (d), we investigate the channel behavior associated with these seemingly similar fluid states and demonstrate how they can lead to significantly different outcomes in multi-user scenarios. Notably, even similar fluid states, such as Tx1: 000000, Tx2: 000000, Rx: 000000 versus Tx1: 000100, Tx2: 000100, Rx: 000100, as can be seem from the near-field patters in Figure 5, which can exhibit completely different SIR performance. This observation highlights the high spatial selectivity and sensitivity of the proposed system, where small changes in pixel configurations can lead to significantly different interference characteristics, enabling fine-grained control for interference mitigation.

IV. Multi-User Interference Mitigation Performance

To evaluate the key novelty of the proposed wideband PB-FAS, this section investigates its ability to mitigate interference in a multi-source downlink scenario, here is two-source downlink case. Both full-wave simulation and experimental validation are presented to demonstrate the effectiveness of radiation state reconfiguration in improving signal quality.

A. SINR Performance by Full-Wave Simulation

A simulated wireless communication setup is constructed in which two transmitters (Tx1 and Tx2) and one receiver

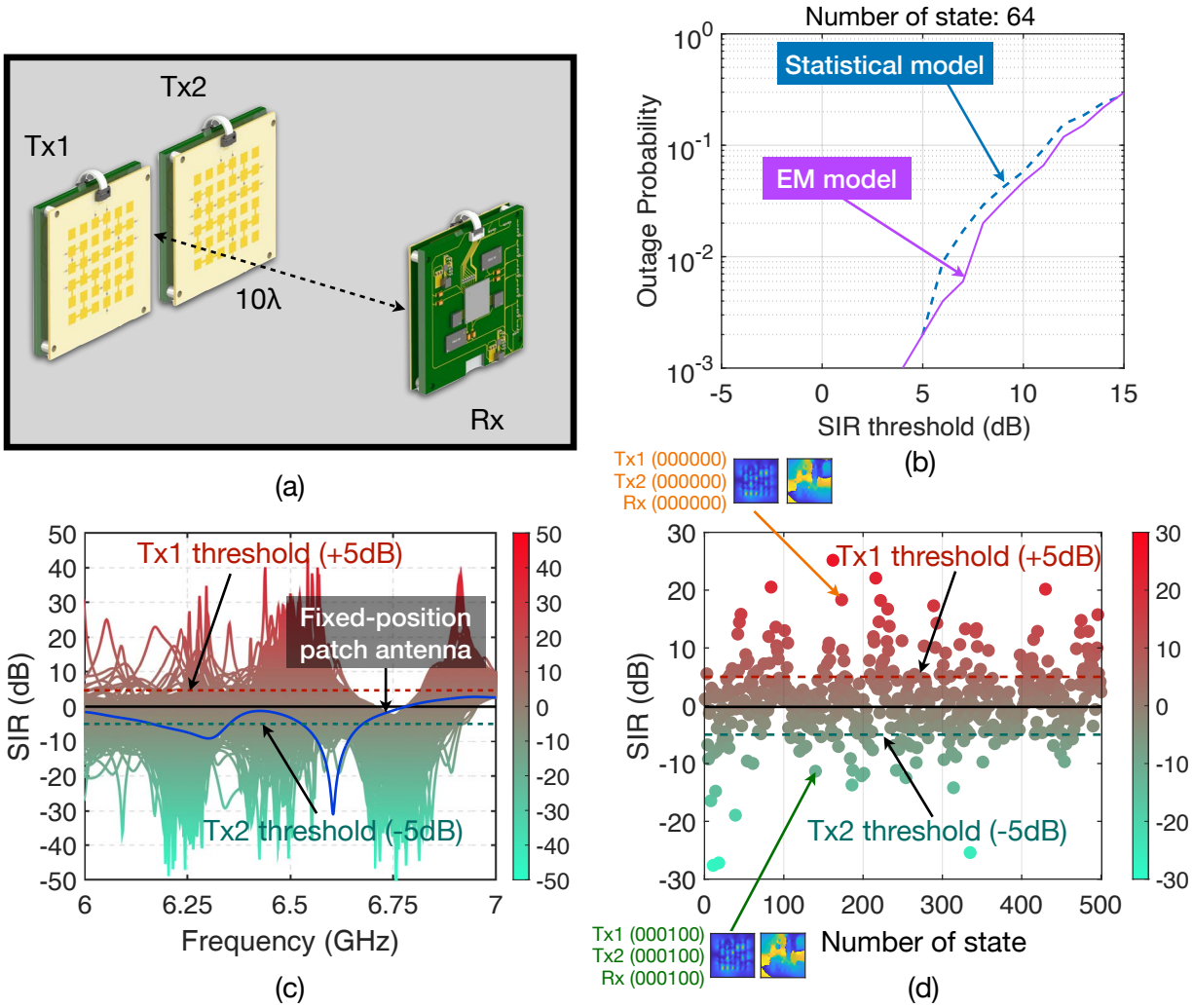

Fig. 7. Performance evaluation of the proposed PB-FAS system using both theoretical modeling and full-wave simulation. (a) Simulation setup used for both theoretical and full-wave electromagnetic analysis, involving two transmitters (Tx1, Tx2) and one receiver (Rx), each equipped with a PB-FAS. (b) Outage probability versus SIR threshold derived from the statistical and EM channel models, the number of states is 64 in this case, only the receiver's state is reconfigured. (c) Simulated wideband SIR performance from 6 to 7 GHz across 500 randomly selected Tx1–Tx2–Rx state combinations, all the transmitters' and the receiver's state are reconfigured. For comparison, the SIR performance of a fixed-position patch antenna is also shown, demonstrating poor isolation and no spatial multiplexing capability. (d) SIR distribution at 6.5 GHz, showing successful interference suppression in a significant portion of the tested states based on the defined SIR thresholds of +5 dB for Tx1 and –5 dB for Tx2. Notably, even similar fluid states, such as Tx1: 000000, Tx2: 000000, Rx: 000000 versus Tx1: 000100, Tx2: 000100, Rx: 000100, can exhibit completely different SIR performance, highlighting the system's spatial selectivity.

(Rx) are each equipped with the proposed PB-FAS. Each PB-FAS supports 64 discrete fluid states, resulting in a total of $64^3 = 262{,}144$ possible Tx1–Tx2–Rx state combinations. To capture the system's general behavior without exhaustive computation, 500 random combinations were selected and analyzed using full-wave electromagnetic simulations over the 6–7 GHz frequency range. Since in full-wave simulations do not include noise, the SINR is replaced by the signal-to-interference ratio (SIR).

Figure 7 presents the multi-faceted evaluation. Figure 7 (a) illustrates the overall simulation setup used for both full-wave and theoretical channel modeling. Figure 7 (b) shows the outage probability versus SIR curve derived from the theoretical channel model, using a +5 dB SIR threshold, the number of states is 64 in this case. Figure 7 (c) depicts the simulated wideband SIR performance across 6–7 GHz for the 500 tested configurations. Figure 7 (d) provides a detailed view of SIR distribution at 6.5 GHz as we can see the largest tuning range of SIR occurs at around 6.5 GHz. A pair of states is considered to enable successful separation if one state allows Tx1 to achieve an SIR greater than +5 dB, while the other state suppresses Tx2's interference below –5 dB. These two distinct fluid states enable spatial separation of the two concurrent signals. A significant portion of tested configurations meet this criterion, demonstrating that the proposed PRA can facilitate hardware-level interference suppression through reconfigurable beamforming—without relying on complex MIMO baseband processing.

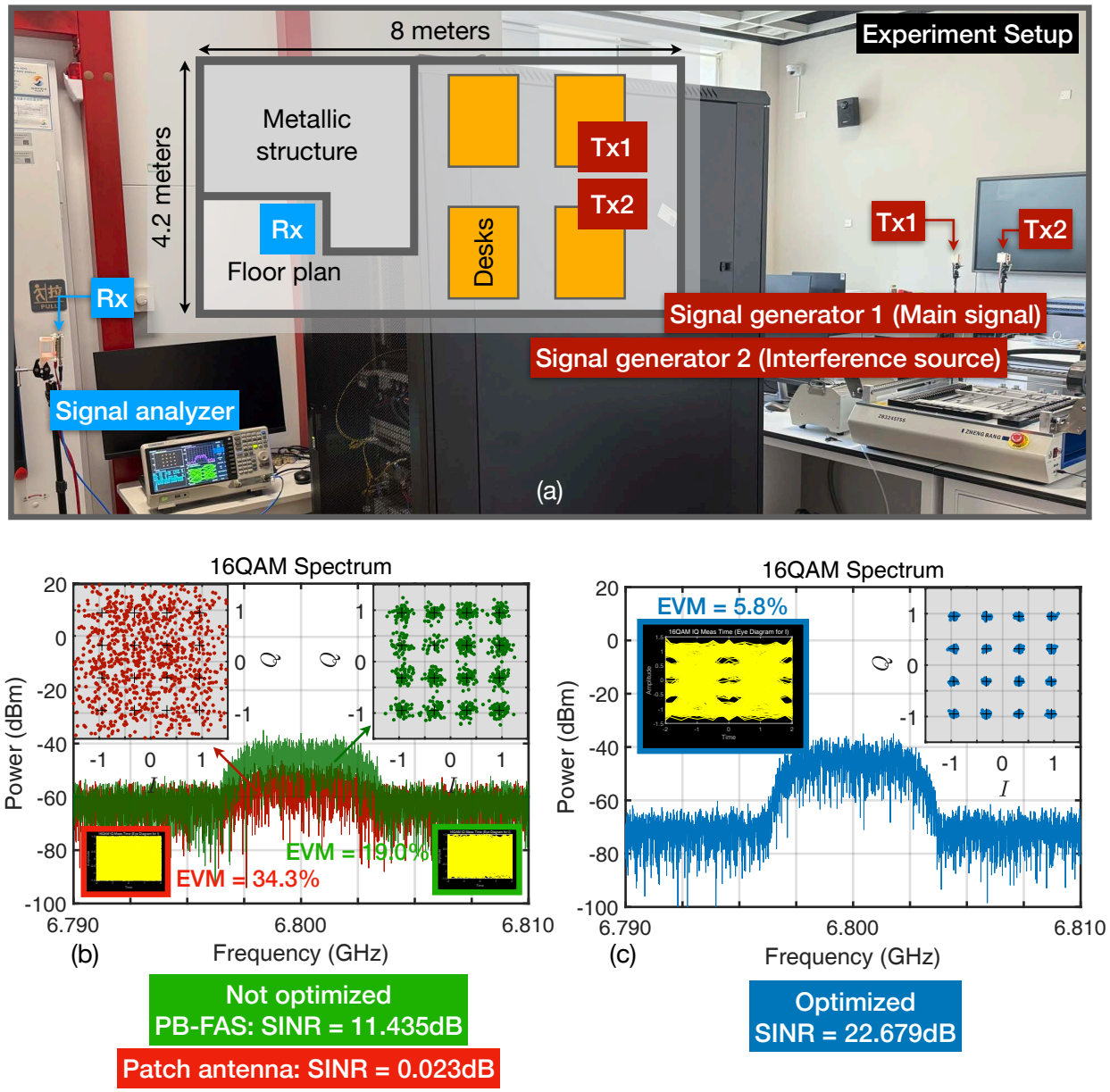

Fig. 8. Measurement setup and performance results for two-source 16-QAM communication in a cluttered indoor environment. (a) illustrates the experimental setup and floor plan. (b) shows the wireless communication data without antenna state optimization, including power level, constellation diagram, and eye diagram. The measured EVM is 19.001% and SINR is 11.435 dB. In order to compare with a conventional antenna setup, the figure also presents baseline results using a standard patch antenna, which exhibits significantly lower performance with an SINR of only 0.023 dB and an EVM of 34.3%. This degradation occurs because the normal antenna receives power indiscriminately from both the desired signal source and the interfering noise source, lacking the spatial selectivity offered by the fluid antenna. (c) presents the optimized case, where the radiation state at the receiver is selected to enhance performance, yielding an EVM of 5.8077% and SINR of 22.679 dB. Measured SINR and EVM performance across 64-fluid states at the receiver, showing up to 11 dB SINR improvement and the EVM is reduced from 19% to 5.8%.

B. Experimental Verification in a Two-Source Rich Scattering Channel

To validate the simulation results in a practical environment, a two-transmitter experiment was conducted in an indoor scenario designed to mimic realistic multipath fading conditions. The experiment took place in a room measuring approximately 8 meters by 4.2 meters, containing desks, walls, and metallic structures that create a rich scattering environment. Both transmitters and the receiver were equipped with the proposed PB-FAS and operated around 6.8 GHz.

One transmitter was connected to an arbitrary waveform generator (AWG) to transmit a 16-QAM signal, representing the desired communication stream. The second transmitter was configured to emit a noise signal, serving as a co-channel interferer. Both the transmitters are sending different signals at the same power level of 10 dBm. At the receiver side, a signal analyzer was used to capture the received signal, perform 16-QAM demodulation, and measure both the signal-to-interference-plus-noise ratio and the error vector magnitude (EVM). To benchmark the performance of the

proposed PB-FAS against a conventional antenna, we also conducted measurements using a standard patch antenna at the receiver. Unlike the reconfigurable PB-FAS, the patch antenna lacks spatial selectivity and thus receives power from both the desired signal source and the interfering noise source. As a result, it exhibits significantly degraded communication quality, with a measured SINR of only 0.023 dB and an EVM of 34.3%, compared to 11.435 dB SINR and 19.001% EVM achieved by the PB-FAS in its unoptimized state. This comparison highlights the fundamental advantage of spatial reconfiguration in mitigating interference without relying on complex signal processing.

By sweeping through the available reconfigurable states of the PB-FAS at all terminals, significant variations in received signal quality were observed. In the best-performing configuration, the SINR improved by up to 11 dB compared to the worst-case scenario. This directly translated into a 13.2 percentage point reduction in EVM during 16-QAM demodulation, as shown in Fig. 8. These results confirm the PB-FAS's capability to mitigate multi-source interference through spatial reconfiguration alone, without requiring any baseband-side channel estimation, equalization, or precoding.

C. Discussion

Base on the aforementioned experiment, this type of wireless communication system demonstrates strong potential for interference mitigation in multi-source environments. By leveraging reconfigurable fluid states at both ends, the system enables one transmitter to deliver a high-power signal to the receiver, while the other transmitter can independently optimize its radiation pattern to minimize interference. This selective spatial control allows different signal sources to coexist within the same frequency band, reducing cross-interference without requiring coordination or complex baseband processing. Such capability is particularly valuable in scenarios like overlapping access points, ambient backscatter networks, and co-channel IoT deployments.

V. Conclusion

This paper presented the design, implementation, and validation of a wideband PB-FAS tailored for sub-7 GHz wireless communication. By incorporating parasitic elements and a reconfigurable pixel surface controlled via PIN diodes, the proposed antenna achieves 64 distinct fluid states with effective impedance matching and dynamic beam forming capability. Full-wave simulations and measurements confirmed the antenna's ability to significantly modify its radiation characteristics and reflection properties in real-time. Both simulation and experimental results in a two-source downlink scenario demonstrated that adaptive radiation state reconfiguration can provide substantial performance gains, achieving up to 11 dB SINR improvement and 13.2% EVM reduction without the need for multiple RF chains or complex signal processing. These results highlight the effectiveness of antenna-level diversity for interference mitigation and channel quality enhancement. Given its compact form factor, low switching complexity, and real-time adaptability, the proposed PRA technology shows strong potential for future massive connectivity applications, especially in IoT deployments and deep fading wireless environments. It offers a scalable and energy-efficient alternative to conventional MIMO systems, paving the way for low-cost, interference-resilient communication in next-generation wireless networks.

Simulation and measurement

All full-wave simulations in this work were conducted using CST Microwave Studio 2024, while channel modeling, signal processing and performance evaluations such as SIR and EVM calculations were carried out in MATLAB 2024. The pixel-based antenna was fabricated using standard printed circuit board (PCB) technology. S-parameters, as well as far-field radiation characteristics, were measured in an anechoic chamber and a Keysight N5224A vector network analyzer. For the wireless communication experiments, two Keysight N5183B signal generators were used to generate the 16-QAM signal and interference, while a Keysight N9010B signal analyzer was employed at the receiver to demodulate the signal and measure SINR and EVM performance.

References

[1] X. You, C.-X. Wang, J. Huang, X. Gao, Z. Zhang, M. Wang, Y. Huang, C. Zhang, Y. Jiang, J. Wang *et al.*, "Towards 6g wireless communication networks: Vision, enabling technologies, and new paradigm shifts," *Sci. China Inf. Sci.*, vol. 64, pp. 1–74, 2021.

[2] W. Khalid *et al.*, "Advanced physical-layer technologies for beyond 5g wireless communication networks," p. 3197, 2021.

[3] D. Wang, X. You, Y. Huang, W. Xu, J. Li, P. Zhu, Y. Jiang, Y. Cao, X. Xia, Z. Zhang *et al.*, "Full-spectrum cell-free ran for 6g systems: System design and experimental results," *Sci. China Inf. Sci.*, vol. 66, no. 3, p. 130305, 2023.

[4] S. Elmeadawy and R. M. Shubair, "Enabling technologies for 6g future wireless communications: Opportunities and challenges," *arXiv preprint arXiv:2002.06068*, 2020.

[5] G.-B. Wu, J. Y. Dai, Q. Cheng, T. J. Cui, and C. H. Chan, "Sideband-free space–time-coding metasurface antennas," *Nat. Electron.*, vol. 5, no. 11, pp. 808–819, 2022.

[6] G.-B. Wu, J. Y. Dai, K. M. Shum, K. F. Chan, Q. Cheng, T. J. Cui, and C. H. Chan, "A universal metasurface antenna to manipulate all fundamental characteristics of electromagnetic waves," *Nat. Commun.*, vol. 14, no. 1, p. 5155, 2023.

[7] B. Liu, K.-F. Tong, K.-K. Wong, C.-B. Chae, and H. Wong, "Programmable meta-fluid antenna for spatial multiplexing in fast fluctuating radio channels," *Opt. Express*, vol. 33, no. 13, pp. 28 898–28 915, 2025.

[8] H. L. Wang, H. F. Ma, M. Chen, S. Sun, and T. J. Cui, "A reconfigurable multifunctional metasurface for full-space control of electromagnetic waves," *Adv. Funct. Mater.*, vol. 31, no. 25, p. 2100275, 2021.

[9] Y. H. Liu, Z. T. Zhang, X. K. Zeng, X. H. Tian, K. N. Qi, Z. R. Ren, S. Y. Wang, and Y. B. Li, "Ultra-wideband intelligent reflectarray for dynamic mimicking the electromagnetic scattering signals," *Adv. Funct. Mater.*, p. 2504200, 2025.

[10] H. Lu, J. Zhao, P. Zhu, W. Song, S. Zhu, R. Zhu, B. Zheng, and H. Chen, "Neural network-assisted metasurface design for broadband remote invisibility," *Adv. Funct. Mater.*, p. 2506085, 2025.

[11] J. Tian, X. Cao, H. Yang, T. Li, and S. Li, "Multi-domain detection computational imaging via reconfigurable metasurfaces mimo system," *Adv. Mater. Interfaces*, vol. 11, no. 9, p. 2300068, 2024.

[12] Z. Wang, J. Zhang, H. Du, W. E. Sha, B. Ai, D. Niyato, and M. Debbah, "Extremely large-scale mimo: Fundamentals, challenges, solutions, and future directions," *IEEE Wireless Commun.*, vol. 31, no. 3, pp. 117–124, 2023.

[13] Z. Wang, J. Zhang, H. Du, D. Niyato, S. Cui, B. Ai, M. Debbah, K. B. Letaief, and H. V. Poor, "A tutorial on extremely large-scale mimo for 6g: Fundamentals, signal processing, and applications," *IEEE Commun. Surv. Tutor.*, vol. 26, no. 3, pp. 1560–1605, 2024.

[14] B. Liu, K.-F. Tong, K.-K. Wong, C.-B. Chae, and H. Wong, "Be water, my antennas: Riding on radio wave fluctuation in nature for spatial multiplexing using programmable meta-fluid antenna," *arXiv preprint arXiv:2502.04693*, 2025.

[15] W. K. New *et al.*, "A tutorial on fluid antenna system for 6g networks: Encompassing communication theory, optimization methods and hardware designs," *IEEE Commun. Surv. Tutor.*, 2024.

[16] K.-K. Wong, A. Shojaeifard, K.-F. Tong, and Y. Zhang, "Fluid antenna systems," *IEEE Trans. Wireless Commun.*, vol. 20, no. 3, pp. 1950–1962, Mar. 2021.

[17] P. Lotfi, S. Soltani, and R. D. Murch, "Printed endfire beam-steerable pixel antenna," *IEEE Transactions on Antennas and Propagation*, vol. 65, no. 8, pp. 3913–3923, 2017.

[18] F. Jiang, C.-Y. Chiu, S. Shen, Q. S. Cheng, and R. Murch, "Pixel antenna optimization using n -port characteristic mode analysis," *IEEE Transactions on Antennas and Propagation*, vol. 68, no. 5, pp. 3336–3347, 2020.

[19] L. N. Pringle, P. H. Harms, S. P. Blalock, G. N. Kiesel, E. J. Kuster, P. G. Friederich, R. J. Prado, J. M. Morris, and G. S. Smith, "A reconfigurable aperture antenna based on switched links between electrically small metallic patches," *IEEE Transactions on Antennas and Propagation*, vol. 52, no. 6, pp. 1434–1445, 2004.

[20] J. Zhang, J. Rao, Z. Li, Z. Ming, C.-Y. Chiu, K.-K. Wong, K.-F. Tong, and R. Murch, "A novel pixel-based reconfigurable antenna applied in fluid antenna systems with high switching speed," *IEEE Open Journal of Antennas and Propagation*, vol. 6, no. 1, pp. 212–228, Feb. 2025.

[21] Y. Shen, B. Tang, S. Gao, K.-F. Tong, H. Wong, K.-K. Wong, and Y. Zhang, "Design and implementation of mmwave surface wave enabled fluid antennas and experimental results for fluid antenna multiple access," *arXiv preprint arXiv:2405.09663*, 2024.

[22] L. Zhu *et al.*, "A tutorial on movable antennas for wireless networks," *IEEE Commun. Surv. Tutor.*, 2025, early access.

[23] B. Liu *et al.*, "Meta fluid antenna: Architecture design, performance analysis, experimental examination," *arXiv preprint*, 2025, arXiv:2509.12032.

[24] X. Lai, J. Yao, K. Zhi, T. Wu, D. Morales-Jimenez, and K.-K. Wong, "Fas-ris: A block-correlation model analysis," *IEEE Trans. Veh. Technol.*, 2024.

[25] J. Yao *et al.*, "Fas-ris communication: Model, analysis, and optimization," *IEEE Trans. Veh. Technol.*, 2025.

[26] H. Xu, G. Zhou, K.-K. Wong, W. K. New, C. Wang, C.-B. Chae, R. Murch, S. Jin, and Y. Zhang, "Channel estimation for fas-assisted multiuser mmwave systems," *IEEE Commun. Lett.*, vol. 28, no. 3, pp. 632–636, 2024.

[27] F. R. Ghadi, K.-K. Wong, C.-B. Chae, R. Murch, S. Jin, and A. Sharples, "Copula-based performance analysis for fluid antenna systems under arbitrary fading channels," *IEEE Commun. Lett.*, vol. 27, no. 11, pp. 3068–3072, 2023.

[28] W. K. New, K.-K. Wong, H. Xu, K.-F. Tong, and C.-B. Chae, "An information-theoretic characterization of mimo-fas: Optimization, diversity-multiplexing tradeoff and q-outage capacity," *IEEE Trans. Wireless Commun.*, vol. 23, no. 6, pp. 5541–5556, 2024.

[29] N. Waqar, K.-K. Wong, K.-F. Tong, A. Sharples, and Y. Zhang, "Deep learning enabled slow fluid antenna multiple access," *IEEE Commun. Lett.*, vol. 27, no. 3, pp. 861–865, 2023.

[30] C. Wang, G. Li, H. Zhang, K.-K. Wong, Z. Li, D. W. K. Ng, and C.-B. Chae, "Fluid antenna system liberating multiuser mimo for isac via deep reinforcement learning," *IEEE Trans. Wireless Commun.*, vol. 23, no. 9, pp. 10 879–10 894, 2024.

[31] T. Wu, K. Zhi, J. Yao, X. Lai, J. Zheng, H. Niu, M. Elkashlan, K.-K. Wong, C.-B. Chae, Z. Ding *et al.*, "Fluid antenna systems enabling 6g: Principles, applications, and research directions," *arXiv preprint arXiv:2412.03839*, 2024.

[32] K.-F. Tong, B. Liu, and K.-K. Wong, "Designs and challenges in fluid antenna system hardware," *Electronics*, vol. 14, no. 7, p. 1458, 2025.

[33] H. Hong, K.-K. Wong, H. Xu, Y. Xu, H. Shin, R. Murch, D. He, and W. Zhang, "Downlink ofdm-fama in 5g-nr systems," *IEEE Trans. Wireless Commun.*, 2025.

[34] X. Lin, Y. Zhao, H. Yang, J. Hu, and K.-K. Wong, "Fluid antenna multiple access assisted integrated data and energy transfer: Outage and multiplexing gain analysis," *IEEE Trans. Wireless Commun.*, 2025.

[35] T. Han, Y. Zhu, K.-K. Wong, G. Zheng, and H. Shin, "Cell-free fluid antenna multiple access networks," *IEEE Trans. Wireless Commun.*, 2025.

[36] B. Feng, C. Feng, K.-K. Wong, and T. Q. Quek, "Deep unfolding neural networks for fluid antenna-enhanced vehicular communication," *IEEE Trans. Veh. Technol.*, 2025.

[37] J. Yao, L. Xin, T. Wu, M. Jin, K.-K. Wong, C. Yuen, and H. Shin, "Fas for secure and covert communications," *IEEE Internet Things J.*, 2025.

[38] K. C. Rath, A. Khang, and D. Roy, "The role of internet of things (iot) technology in industry 4.0 economy," in *Advanced IoT technologies and applications in the industry 4.0 digital economy*. CRC Press, 2024, pp. 1–28.

[39] S. Douhi, Z. Zakaria, M. Idiri, and A. Eddiai, "Design and simulation of a flexible uwb mimo antenna for mm-wave iot applications: Performance and sar evaluation," *Adv. Theory Simul.*, p. 2500075, 2025.

[40] J. Huang, H. Meng, L. Ning, B. Liu, K.-K. Wong, K.-F. Tong, and H. Wong, "Meta-fluid antenna for multiplexing multiple users in rich scattering environments," in *2024 IEEE 10th International Symposium on Microwave, Antenna, Propagation and EMC Technologies for Wireless Communications (MAPE)*. IEEE, 2024, pp. 1–4.

[41] Z. Dong, Z. Zhou, Z. Xiao, C. Zhang, X. Li, H. Min, Y. Zeng, S. Jin, and R. Zhang, "Movable antenna for wireless communications: Prototyping and experimental results," *arXiv preprint arXiv:2408.08588*, 2024.

[42] H. O. Y. Suzuki and K. Kawai, "Pinching antenna: Using a dielectric waveguide as an antenna," *NTT DOCOMO Technical J*, vol. 23, no. 3, pp. 5–12, 2022.